nature communications

Article

https://doi.org/10.1038/s41467-024-53656-w

Motorless transport of microtubules along tubulin, RanGTP, and salt gradients

Received: 22 March 2024

Accepted: 16 October 2024

Suin Shim[1], Bernardo Gouveia[2], Beatrice Ramm[3,4], Venecia A. Valdez[4], Sabine Petry[4] & Howard A. Stone[1]

Microtubules are dynamic filaments that assemble spindles for eukaryotic cell division. As the concentration profiles of soluble tubulin and regulatory proteins are non-uniform during spindle assembly, we asked if diffusiophoresis - motion of particles under solute gradients - can act as a motorless transport mechanism for microtubules. We identify the migration of stable microtubules along cytoplasmic and higher concentration gradients of soluble tubulin, $MgCl_2$, Mg-ATP, Mg-GTP, and RanGTP at speeds $O(100)$ nm/s, validating the diffusiophoresis hypothesis. Using two buffers (BRB80 and CSF-XB), microtubule behavior under $MgCl_2$ gradients is compared with negatively charged particles and analyzed with a multi-ion diffusiophoresis and diffusioosmosis model. Microtubule diffusiophoresis under gradients of tubulin and RanGTP is also compared with the charged particles and analyzed with a non-electrolyte diffusiophoresis model. Further, we find that tubulin and RanGTP display concentration dependent cross-diffusion that influences microtubule diffusiophoresis. Finally, using *Xenopus laevis* egg extract, we show that diffusiophoretic transport occurs in an active cytoplasmic environment.

The non-uniform and out-of-equilibrium nature of the intracellular environment is of interest among various fields of science. In particular, the question of motorless transport following concentration gradients of smaller species has been raised often by the biocommunities[1–5]. In colloid science, the spontaneous movement of particles along solute gradients is called diffusiophoresis. Although it sounds like the independent motion of point-like particles, the phenomenon is in fact driven at the nanoscale by the movement of liquid adjacent to the particle surface. After its discovery (1947)[6] and introduction to a broader community (1980–90s)[7–16], diffusiophoresis has been suggested occasionally as an intracellular transport mechanism[17] (e.g., for membrane cargos under MinDE protein gradients[18] and for chemically active and passive liquid condensates[19]). However, due to the complexity of the phenomenon and difference in the scales of interest among disciplines, the possibility of diffusiophoresis in the cytoplasm has not been directly proven. The complex cytoplasmic environment itself is also a hurdle for initiating such an investigation. In order to determine whether there is intracellular diffusiophoresis, it is essential to identify an overlapping regime where both theoretical and experimental approaches to diffusiophoresis, utilizing realistic biological parameters, are applicable. Therefore, we chose the well-known scene of spindle assembly as the motivation for the current study.

Spindle assembly is a core element of cell division in eukaryotic cells, where microtubules (MTs) form both mitotic and meiotic spindles during the cell cycle. Spindle MTs are formed by tubulin dimers polymerizing into hollow cylindrical structures with an outer diameter of 25 nm and a length of $O(1–10)$ µm[20,21]. In order to build MTs, there is accumulation of soluble tubulin above a critical concentration near certain nucleation sites, e.g., centrosomes during mitosis[22–24] or branch sites[25]. Upon nucleation, MTs in spindles can grow and shrink, while also being transported throughout the spindle[26,27]. Besides tubulin, other macromolecules are also non-uniformly distributed during spindle assembly[25,28–33]. Perhaps best characterized for its gradient is

---

[1]Department of Mechanical and Aerospace Engineering, Princeton University, Princeton, NJ, USA. [2]Department of Chemical and Biological Engineering, Princeton University, Princeton, NJ, USA. [3]Department of Physics, Princeton University, Princeton, NJ, USA. [4]Department of Molecular Biology, Princeton University, Princeton, NJ, USA. e-mail: sshim@princeton.edu; hastone@princeton.edu

Ran (Ras-related nuclear protein), which is loaded with GTP at chromosomes to become active, a state in which it releases spindle assembly factors (SAFs) from importins. Away from chromosomes, RanGTP activates RanGAP to hydrolyze GTP. As a result, active Ran and its downstream SAFs exist in a gradient around chromosomes[34–39]. While it is now well known that tubulin accumulation at MT organizing centers is directly relevant for MT nucleation, and that the RanGTP gradient leads to a gradient of released SAFs that facilitates spindle assembly, it has not been explored whether these non-uniform distributions can have a direct effect on the movement of MTs, i.e., by contrast with movement by molecular motors.

Chemical gradients are known to influence colloidal transport processes widely, e.g., chemotaxis, isotachophoresis, diffusiophoresis, osmophoresis, etc.[40–43]. In particular, diffusiophoresis is a physicochemical hydrodynamic phenomenon driven by the osmotic pressure gradient and the corresponding slip flow generated at an interaction length scale along a surface[6,8,10,12,13,15,16,42,44–46]. Therefore, in order to identify a certain transport process as diffusiophoresis, integrated analyses of the coupled movements of background solutes, particles, and the surrounding fluid are necessary. In studies in colloid science, diffusiophoresis is widely investigated for micron-sized particles, as the typical diffusiophoretic mobility along a salt (e.g., NaCl) gradient is about a thousand times larger than the particles' Stokes-Einstein diffusivity[42,47–49]. As a number of gradients exist in the spindle and given the size of MTs being $O(1–10)$ µm, it is critical to investigate whether diffusiophoresis can be present during spindle assembly.

Within the past decade, various particles[18,49–59] and solutes[18,60–64] have been demonstrated for diffusiophoresis. In particular, diffusiophoresis of biological particles has been of interest due to the ubiquity of solute gradients in biological systems. Under laboratory conditions, it has been visualized that cells[49,53,65,66], DNA[54], vesicles[55], and proteins[56–58] can undergo diffusiophoresis. Also, using the E. coli MinDE system as a model, it has been demonstrated that protein gradients can drive diffusiophoretic transport of cargos on biological membranes[5,18]. On the other hand, it has been suggested with numerical calculations that diffusiophoresis could be present in cells[17,19] or influence pattern formation in biosystems[67]. To the best of our knowledge, there has not been any direct comparison between experiments and theory that quantitatively assessed diffusiophoresis of cytoplasmic particles (or macromolecules) under cytoplasmic solute gradients.

In this article, we identify and document the diffusiophoretic behavior of stable MTs (so-called MT seeds). By comparing the microfluidic experiments with the models considering both electrolyte- and non-electrolyte-driven diffusiophoresis, we suggest that diffusiophoresis is a non-equilibrium, passive transport mechanism for MTs, with applications for spindle assembly and other intracellular migration. For systematic validation, MT interactions with all species in the system are quantified, and we show that diffusiophoresis can occur in an active cytoplasmic environment (*Xenopus laevis* egg extract).

Results and discussion

Microtubules migrate along a micromolar concentration gradients of tubulin

We use a microfluidic channel with a dead-end pore geometry (Fig. 1a) to create a one-dimensional (1D) concentration gradient of solutes and observe the response of stabilized MTs ($\lesssim 10$ µm). Dead-end pores are first filled with a buffer (BRB80 or CSF-XB; see Methods for details), then followed by an air bubble. MTs, which are suspended in the matching buffer with various concentrations of soluble tubulin, are flowed into the main channel and connected to the liquid in the pores. All MTs used in this study are tagged with Alexa Fluor 568. Soluble tubulin used to create the concentration gradient is untagged and does not contribute to MT polymerization, as there is no GTP or GTP-analog in the final buffer (see Methods for details). We observe that MTs move into the dead-end pores, down the tubulin gradient (Fig. 1b, c and Fig. E1; see SI). Considering the size of the MTs (25 nm in diameter and $\lesssim 10$ µm in length), we can rule out-diffusion ($O(10^{-13})$ m^2/s) as the cause of entrainment.

Several aspects of MT entrainment are noteworthy. First, MTs move into the pores at typical speeds of 0.1–0.4 µm/s, which depend on the tubulin concentration. Second, the entrainment behavior changes when a different buffer is used. Third, the entrainment front is not a flat boundary but instead has a parabolic shape, which indicates that the speed of MTs is not uniform across the pore. From these observations, we reach a qualitative conclusion that the tubulin-gradient-driven transport of MTs is diffusiophoresis, and the non-uniform entrainment front is due to the diffusioosmotically induced liquid flow[68–70] along the boundaries of the pores. The liquid flow velocity (v_F) induced by the wall diffusioosmosis (v_S) reflects the geometry of the pores (Fig. 1d, eqn. (S1)), and thus the rescaled velocity profile (v_F/v_S) can be plotted versus the cross-sectional axis (Fig. 1d). The entrainment front corresponds to the fastest MTs following $v_F(z=0)$, and, for pores with width and height, respectively, $w = 100$ µm and $h = 50$ µm, we find $v_F(z=0) = 0$ at $y = \pm 39.9$ µm (Fig. 1d(ii)). This means that in all of our experiments, the MT speed has only the phoretic component along $y \approx 40$ µm, and thus we plot the front distance along $y = 40$ µm versus time to quantify the tubulin-driven diffusiophoresis of MTs (Fig. 1e, f). In both BRB80 and CSF-XB solutions, MTs move further into the pores under a larger tubulin concentration gradient.

These findings pose the following questions. How is protein-driven diffusiophoresis possible in a buffer environment? Specifically, we are not aware of any previous study that recognized MTs could even undergo diffusiophoresis. Moreover, in contrast to electrolyte solutions, studies of non-electrolyte-driven diffusiophoresis are few in number. To characterize this phenomenon, we next perform a step-by-step approach to establish the mechanism of MT transport by diffusiophoresis.

$MgCl_2$-driven diffusiophoresis of microtubules

In order to understand how MTs can undergo diffusiophoresis when interacting with simple ions and buffering agents, we studied MTs and carboxylate-modified polystyrene (c-PS; diameter $d = 1$ µm) particles in $MgCl_2$ gradients in BRB80 buffer. In our experiments, we investigate electrolyte-driven diffusiophoresis systematically by comparing the experiments with a model of multi-ion diffusiophoresis and diffusioosmosis. Both MTs and c-PS particles have a negative surface potential[71–73] (see SI), and the direction of transport depends on the diffusivity difference factor $\beta = \frac{D_+ - D_-}{z_+ D_+ - z_- D_-}$, where D_+, D_- and z_+, z_- are, respectively, the diffusion coefficients and valences of cations and anions[74]. For $MgCl_2$, $\beta = -0.385$ from which it follows that negatively charged particles always migrate up the gradient of $MgCl_2$. Thus, we predict that the direction of MT migration is towards higher concentrations of $MgCl_2$.

We set up the $MgCl_2$ experiments by initially filling the pores with a solution of BRB80 and $MgCl_2$ (Fig. 2a). BRB80 buffer contains 1 mM of $MgCl_2$, and thus the gradient is established by fixing the $MgCl_2$ concentration in the pores at 10, 25, 50, 75, and 100 mM. As the stream of MTs (or c-PS particles) connects with the liquid in the pores, MTs (or c-PS) start to move into the pores by diffusiophoresis (Fig. 2b–d). We observed that the behavior of MTs (Fig. 2b) is analogous to that of c-PS particles (Fig. 2d), yet there can be a question about the orientation of MTs. The MT suspension is dilute and MTs are much smaller than the pores (see SI for MT characterization). Also, the MTs experience rotation by Brownian motion and the non-uniform flow velocity inside the pores. Consequently, we expect no preferred orientation of MTs outside the wall region, as shown in higher magnification images (Fig. 2c) and the corresponding movie (Supplementary Movie 1). The squared entrainment distance (along

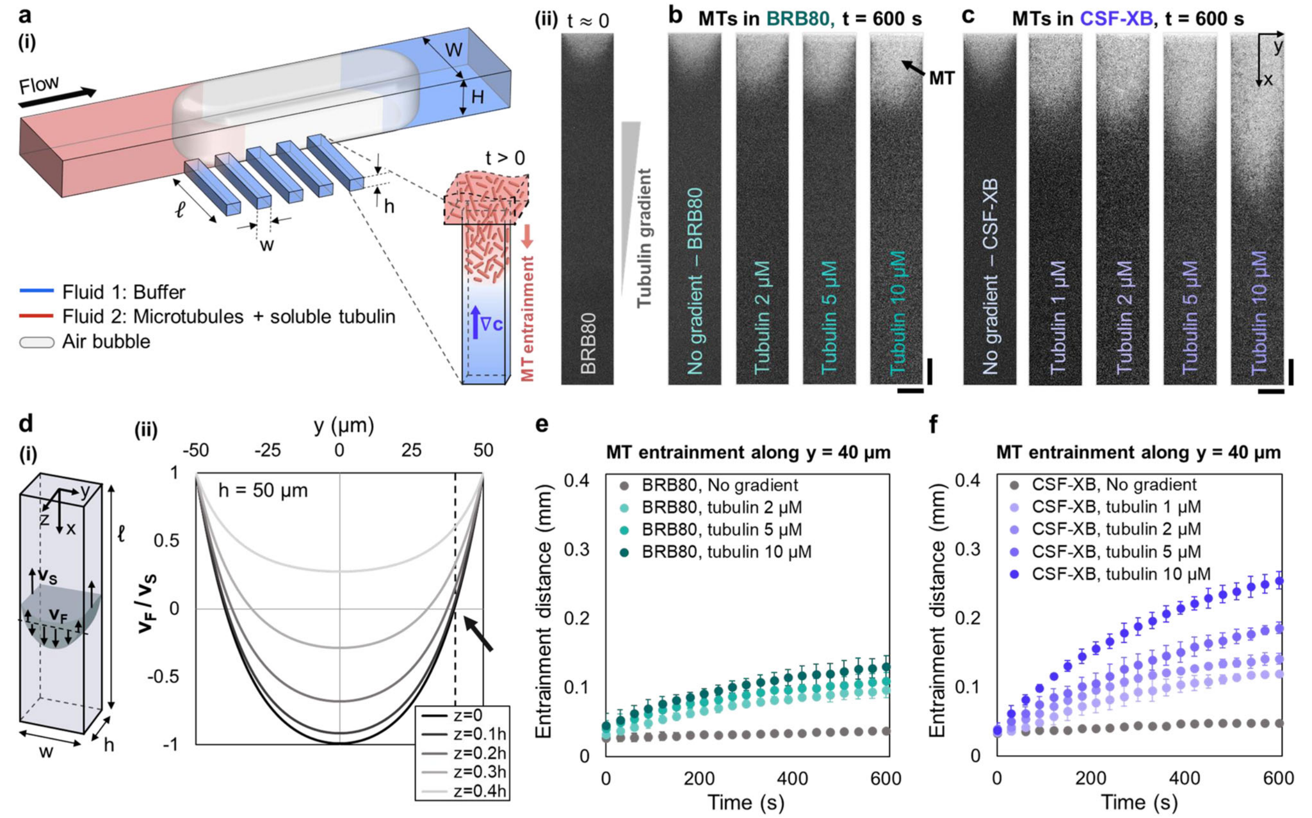

Fig. 1 | Concentration dependent migration of microtubules (MTs) under various gradients of soluble tubulin. a(i) Schematic of experimental setup with a microfluidic dead-end pore geometry. The dimensions of the main channel and dead-end pores are, respectively, $W = 750$ μm, $H = 150$ μm and $L = 5$ cm; $w = 100$ μm, $h = 50$ μm and $\ell = 1$ mm. **a(ii)** A pore image at $t \approx 0$ (immediately after the two liquids merged) for the experimental condition with BRB80 and 10 μM tubulin gradient. MTs migrating under a range of tubulin gradients in (**b**) BRB80 and (**c**) CSF-XB buffers. Time sequence of the images for 5 μM tubulin gradient is included in Fig. E1 (see SI). **b**, **c** The tubulin gradient not only drives migration of MTs (diffusiophoresis), but also generates a slip flow along the pore walls (diffusioosmosis), inducing liquid flow inside the pore. The local flow velocity at different cross-sectional positions makes the MTs move at different speeds along the x-axis, making the entrainment front a parabolic shape. **d** The flow velocity (rescaled by the slip velocity; v_F/v_S) is plotted versus y, for different z positions. We consider v_F ($z = 0$) when analyzing the front trajectories. For the pores with $w = 100$ μm and $h = 50$ μm, $v_F(z = 0) = 0$ at $y = \pm 39.9$ μm. Therefore, the measured front trajectories along $y = 40$ μm can be assumed only the tubulin-driven migration of MTs. The average entrainment distances measured along $y = 40$ μm are plotted versus time for (**e**) BRB80 ($n = 16$ pores) and (**f**) CSF-XB ($n = 23$ pores), for different tubulin concentration gradients. All error bars indicate standard deviation (SD). Scale bars are 50 μm.

$y = 40$ μm) linearly increases with time (Fig. 2e), showing the diffusive nature of diffusiophoresis.

For quantitative analysis, we considered multi-ion diffusiophoresis and diffusioosmosis so that two-dimensional (2D) experimental data can be directly compared with 1D calculations. The influence of background ions is significant (Fig. S1), and thus consideration of all ions in the electrokinetic modeling is necessary. For the combination of negatively charged particles and $MgCl_2$ gradients, both the electrophoretic and chemiphoretic contributions to diffusiophoresis are in the direction of the positive $MgCl_2$ gradient (Fig. 2b). Channel walls are also negatively charged[75], and diffusioosmotic flow is generated in the $-x$ direction. The sum of the diffusiophoretic and local flow velocities is the advective velocity of each MT (Fig. S2).

The multi-ion model considers coupled diffusion of all species (K^+, $PIPES^{2-}$, $PIPES^-$, Mg^{2+}, and Cl^-; see SI for details) in the system. The 1D transport of ions of species i of concentration $c_i(x, t)$ is described with the Nernst-Planck equation (the x axis is defined from the pore inlet),

$$\frac{\partial c_i}{\partial t} = D_i \frac{\partial^2 c_i}{\partial x^2} + \frac{D_i z_i e}{k_B T} \frac{\partial}{\partial x}\left(c_i \frac{\partial \psi}{\partial x}\right). \tag{1}$$

Here, z_i, ψ, k_B, T, and e are, respectively, the valence of the ith ion, electric potential, Boltzmann constant, absolute temperature, and the element charge. The initial and boundary conditions are $c_i(x, 0) = c_{ip}$, $c_i(0, t) = c_{ic}$, $\frac{\partial c_i}{\partial x}\big|_{x=\ell} = 0$, where the values for the pore c_{ip} and channel c_{ic} are set to match the experimental conditions. The electroneutrality ($\sum_i z_i c_i = 0$) and zero current ($\sum_i z_i j_i = 0$; $j_i = -D_i\left(\frac{\partial c_i}{\partial x} + \frac{z_i e c_i}{k_B T}\frac{\partial \psi}{\partial x}\right)$) conditions hold. The ionic strength of the BRB80 buffer is $\sum_i z_i^2 c_i = 246$ mM, and the corresponding Debye length is $\lambda_D = \sqrt{\epsilon k_B T/(e^2 \sum_i z_i^2 c_i)} = 0.87$ nm, where ϵ is the dielectric permittivity of the liquid. Therefore, denoting R_{MT} as the outer radius of an MT, then $\lambda_D/R_{MT} \approx 0.07 \ll 1$. This condition allows us to use the diffusiophoretic velocity u_{DP} derived with the assumption of a thin electrical double layer[76],

$$u_{DP}\left(\zeta_p\right) = \frac{\epsilon}{\mu}\left(\frac{k_B T}{e}\right)\frac{\sum_i D_i z_i \frac{\partial c_i}{\partial x}}{\sum_i D_i z_i^2 c_i}\zeta_p + \frac{\epsilon}{8\mu}\frac{\sum_i z_i^2 \frac{\partial c_i}{\partial x}}{\sum_i z_i^2 c_i}\zeta_p^2, \tag{2}$$

where ζ_p is the zeta potential of MTs (or c-PS). u_{DP} is independent of particle shape. For the walls with a zeta potential ζ_w, the diffusioosmotic velocity is $v_s = -u_{DP}(\zeta_w)$ (SI; eqn. (S9)).

We analyzed the entrainment front at five different y-positions ($y_i = 0$, 10, 20, 30, and 40 μm) (Fig. 2f and Fig. S2). Each trajectory ($x_p(t)|_{y=y_i}$) can be calculated with $\frac{dx_p}{dt}\big|_{y=y_i} = u_{DP}(x_p, t) + v_F(x_p, t)|_{y=y_i, z=0}$. Using ζ_p and ζ_w as fitting parameters, the least squares fit is applied

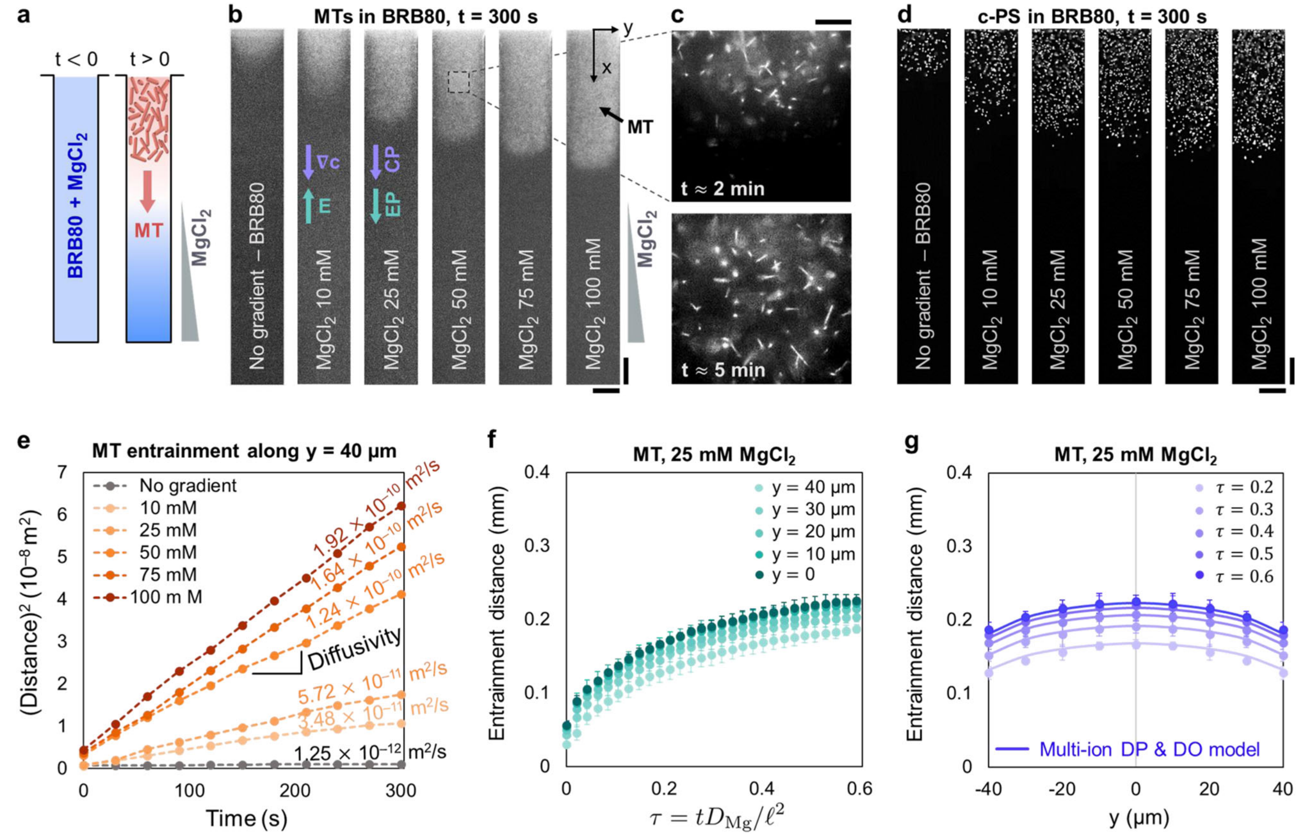

Fig. 2 | Entrainment of microtubules (MTs) and carboxylate-modified polystyrene (c-PS) particles in dead-end pores under various concentration gradients of MgCl$_2$: Multi-ion diffusiophoresis (DP) and diffusioosmosis (DO) in dead-end pores. a Schematic of the MgCl$_2$ experiments. **b** Pore images obtained at 300 s for MTs under different MgCl$_2$ gradients. In BRB80 buffer, the entrainment of MTs depends on the MgCl$_2$ concentration. **c** Images obtained at higher magnification show that the migrating MTs do not have a preferred orientation. **d** Images of c-PS particles under the same MgCl$_2$ gradients. The MT entrainment and c-PS diffusiophoresis under MgCl$_2$ gradients are analogous, and thus we use a multi-ion DP and DO model to analyze both systems. **e** The squared entrainment distances of MTs along $y = 40$ μm are plotted versus time for different MgCl$_2$ concentration gradients. The squared distances are linearly increasing in time, with the slopes indicating the diffusivities of MTs under various conditions. For the no gradient case, the obtained mobility is a combined result of diffusion and flow-driven penetration of particles at the pore inlet[61]. **f** The trajectories of MT entrainment front are plotted versus nondimensional time ($\tau = tD_{\mathrm{Mg}}/\ell^2$) for five y-positions. **g** From the multi-ion DP and DO model, the MT entrainment front is predicted by using the zeta potentials of MTs (ζ_p) and pore walls (ζ_w) as fitting parameters. Least squares fit is applied for 25 data points (five y-positions and five τ points) with $\bar{\zeta}_p, \bar{\zeta}_w = \pm 0.005$. The comparison between MT experiments and model calculations is shown for MgCl$_2$ 25 mM. See Fig. S3 for the comparison for all MgCl$_2$ concentrations (MT). See Fig. S4 for the comparison for c-PS particles in BRB80. See Fig. S6 for the data obtained from CSF-XB and the corresponding model calculations. We used a constant zeta potential assumption, and the experimental data are obtained for $y = 0$, 10, 20, 30, and 40 μm and plotted symmetrically in y. Fitting parameters are listed in Table S1. **e**–**g** All data are presented as mean ± SD ($n = 25$ pores). Scale bars are, respectively, (**b**, **d**) 50 μm and (**c**) 10 μm.

for 25 data points, corresponding to five y-positions and five time points, with $\bar{\zeta}_p, \bar{\zeta}_w = \pm 0.005$ (here $\bar{\zeta}_p = \zeta_p e/k_B T$ and $\bar{\zeta}_w = \zeta_w e/k_B T$ are the nondimensional zeta potentials, and thus with ζ_p, $\zeta_w \approx \pm 0.1$ mV). In Fig. 2g, we show the experimental results and comparison with the model for 25 mM MgCl$_2$. The fitting parameters are $\zeta_p = -35.5$ mV and $\zeta_w = -7.2$ mV. The zeta potential of MTs obtained from our calculations is consistent with a few previously reported values measured electrophoretically[71,72] and calculated theoretically[73] under similar ionic strength conditions. The wall zeta potential for PDMS (polydimethylsyloxane) being $-O(1)$ mV at $O(100)$ mM of background ionic strength is also consistent with the reported range[75]. Comparison between experiments and the model for all MgCl$_2$ concentrations is included in the SI (Fig. S3). We also compared the measurements and calculations for c-PS particles, and the results are included in the SI (Fig. S4). See SI for the data from CSF-XB (Fig. S6). All zeta potential values are listed in Table S1.

From this analysis, we not only estimate the zeta potential of MTs in buffers, but also confirm that the entrainment behavior into a pore is MgCl$_2$-driven diffusiophoresis. MTs and c-PS particles can undergo diffusiophoresis in electrolyte gradients due to their negative surface potential. Next, we further examine the behavior of MTs using Mg-ATP and Mg-GTP salts in CSF-XB.

Mg-ATP- and Mg-GTP-driven diffusiophoresis of MTs

We have confirmed experimentally that both Mg-ATP and Mg-GTP gradients induce diffusiophoresis of MTs (Fig. 3 and Fig. E2; see SI). In the presence of Mg^{2+}, ATP, and GTP predominantly exist as the Mg-complex form both in the cytoplasm and in buffers (binding constant ≈ 10^4 M^{-1})[77–81]. Considering the binding constant and the predominance of the 1:1 complex at pH > 7[77,78,80], we assume that the dissolution of Mg- salts results in the same concentrations of Mg-ATP and Mg-GTP complexes. Since the main source of a concentration gradient is the Mg-complex (not the separate Mg^{2+}, ATP^{4-}, and GTP^{4-}), we cannot use the diffusivity difference factor β to examine the directionality of Mg-ATP- and Mg-GTP-driven diffusiophoresis. Therefore, the directionality of the MT migration is checked experimentally using the compaction (Fig. 3; negative gradients into the pore) and entrainment (Fig. S7; positive gradients into the pore) configurations. In the compaction configuration, a finite amount of MTs is initially located in the pore, and the solute gradients induce MT migration toward the

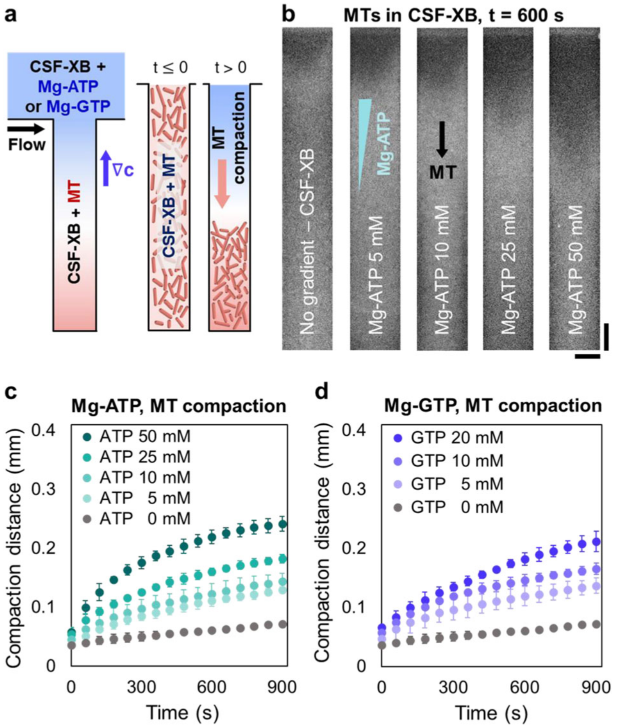

Fig. 3 | Diffusiophoresis of MTs under ATP and GTP gradients in CSF-XB. **a** Schematic of the compaction configuration. We used Mg-ATP and Mg-GTP salts to demonstrate ATP- and GTP-driven diffusiophoresis. MT migration follows the negative concentration gradients of Mg-ATP and Mg-GTP complexes. The compaction configuration is chosen to ensure that MTs and Mg-ATP (or Mg-GTP) contact with each other at $t \gtrsim 0$. **b** MT compaction images obtained at $t = 600$ s for different Mg-ATP concentration gradients. Compaction distances of MTs are plotted versus time for different (**c**) Mg-ATP and (**d**) Mg-GTP concentrations. The images of Mg-GTP experiments are included in Fig. E2 (see SI). All data are presented as mean ± SD ($n = 15$ pores).

dead-end of the pores. This configuration is chosen to ensure that the Mg- complexes and MTs are only in contact with each other for $t > 0$ (see SI and Methods for details), and the compaction profiles as well as the experimental images are shown in Fig. 3b–d and Fig. E2 (see SI). Millimolar concentrations of both Mg-ATP and Mg-GTP complexes drive the motion of MTs along the negative gradients at speeds of $O(0.1)$ µm/s. Similar response of MTs to Mg-ATP and Mg-GTP gradients is expected from the structural similarity between ATP and GTP.

In a recent study[18], an indirect ATP-driven diffusiophoresis is reported for the pattern formation of membrane cargos. ATP is consumed to induce self-organization of MinDE proteins, which further drives the directed motion of cargos. Also, a theoretical study[17] suggests the possibility of ATP-driven diffusiophoresis in cells. Our measurements for the speed of Mg-ATP-driven diffusiophoresis are consistent with the theoretically estimated values[17], and thus our experiments confirm the possibility of the ATP-driven diffusiophoretic mechanism for MTs. When considering ATP or GTP in biological contexts, hydrolysis of ATP and GTP is important to discuss. Another recent article[82] studied the influence of ATP hydrolysis on the phoretic behavior of synthetic colloids (catalytic microbeads). A similar mechanism might apply to MT diffusiophoresis in the presence of ATP/GTP hydrolysis, but this requires separate investigation to identify the coupled interactions of the system components. More detailed discussions on Mg-ATP- and Mg-GTP-driven diffusiophoresis using experiments and model calculations are included in the SI sections 5 and 8. Both ATP and GTP are known to play important roles during mitosis[34–39,83,84] and binding of Mg^{2+} to ATP and GTP is crucial for various intracellular processes[79,81,85]. Therefore, the results shown in Fig. 3, Fig. E2 (see SI), Figs. S7 and S15 are relevant for the motorless transport of MTs.

Diffusiophoresis of MTs under a RanGTP gradient: diffusion of background tubulin

The RanGTP gradient plays a major role in spindle assembly[35–39]. However, can it also affect MT transport? With this motivation in mind, we performed experiments on MTs in increasing and decreasing gradients of purified RanQ69L (a mutant of Ran permanently in its GTP bound form; Fig. 4a) in CSF-XB, using the compaction and entrainment configurations (see Methods for details). Again, for a compaction (entrainment) experiment, a negative (positive) concentration gradient is set up into the pore. We observe that, unlike the previous experiments, MTs migrate along both positive and negative gradients of RanQ69L (Fig. 4b–e). Also, there was only minor concentration dependence in the MT travel distance. Even though both tubulin and RanQ69L are proteins, the response of MTs under the respective gradients looks different. In order to explain such a difference, we looked into the details of the RanQ69L-driven entrainment (Fig. 4f).

With higher contrast, we observe that on top of the entrainment of MTs (Fig. 4f; red arrow), in the background there is spreading of a bright signal (Fig. 4f; blue arrow), which is the depolymerized soluble tubulin from the MT suspension. Such fluorescent background tubulin was rarely detected in the earlier experiments. In our experience, it is only under RanQ69L gradients that the presence of the background tubulin is not negligible (Fig. 4f and Fig. S9b) and, moreover, the diffusion behavior of the background tubulin depends on the concentration of RanQ69L (Fig. 4f). There is no previous study that specifically reported stability of MTs in the presence of RanQ69L in CSF-XB, but it was consistently observed in our experiments that a non-negligible amount of MTs depolymerize in the presence of purified RanQ69L (see Fig. S10 for further characterization). We also tested whether RanQ69L-induced depolymerization of MTs occurs in the seed solutions obtained with a different stabilizer (Taxol; see Methods), and observed consistent background diffusion of depolymerized tubulin in the presence of RanQ69L. As a result, the compaction and entrainment experiments of the Taxol-stabilized seeds performed with a RanQ69L gradient showed similar results to those with the GMPCPP-stabilized MTs (Fig. S11). These findings led us to perform a separate set of experiments observing just the diffusion of soluble tubulin under various solute gradients (Fig. 5).

In the cases with no solute gradient in BRB80 and CSF-XB, a $MgCl_2$ (50 mM) gradient in BRB80, a Mg-ATP (25 mM) gradient in CSF-XB, and a Mg-GTP (25 mM) gradient in CSF-XB, tubulin diffusion did not measurably vary (Fig. 5a), as is shown with the squared entrainment distance versus time plot in Fig. 5c. The squared distance is linear in time, and the slope of the averaged plot ($\approx 10^{-10}$ m^2/s) is a measure of the diffusion coefficient (D_{tub}) of tubulin. From the Stokes-Einstein equation, $D_{tub} = \frac{k_B T}{6\pi\mu R_{tub}}$, we estimate the radius of tubulin to be $R_{tub} \approx 2.2$ nm, which is consistent with previously reported values[86]. We can further conclude from our observations of tubulin diffusion under $MgCl_2$, Mg-ATP, and Mg-GTP gradients (Fig. 5a, c) that the transport of ions and buffering agents are not affected by the tubulin diffusion.

Remarkably, under RanQ69L gradients, tubulin displayed concentration dependent diffusion (Fig. 5b and Fig. E3; see SI). Diffusion profiles at $t = 600$ s for different concentrations of RanQ69L are plotted versus x in Fig. E3 (see SI). It is clearly visible that at higher concentration of RanQ69L there is enhanced diffusion of tubulin along the pore. Concentration-dependent diffusion of biological species is a commonly observed phenomenon[87], but we are not aware of any previous studies reporting such a transport-related interaction between Ran and tubulin.

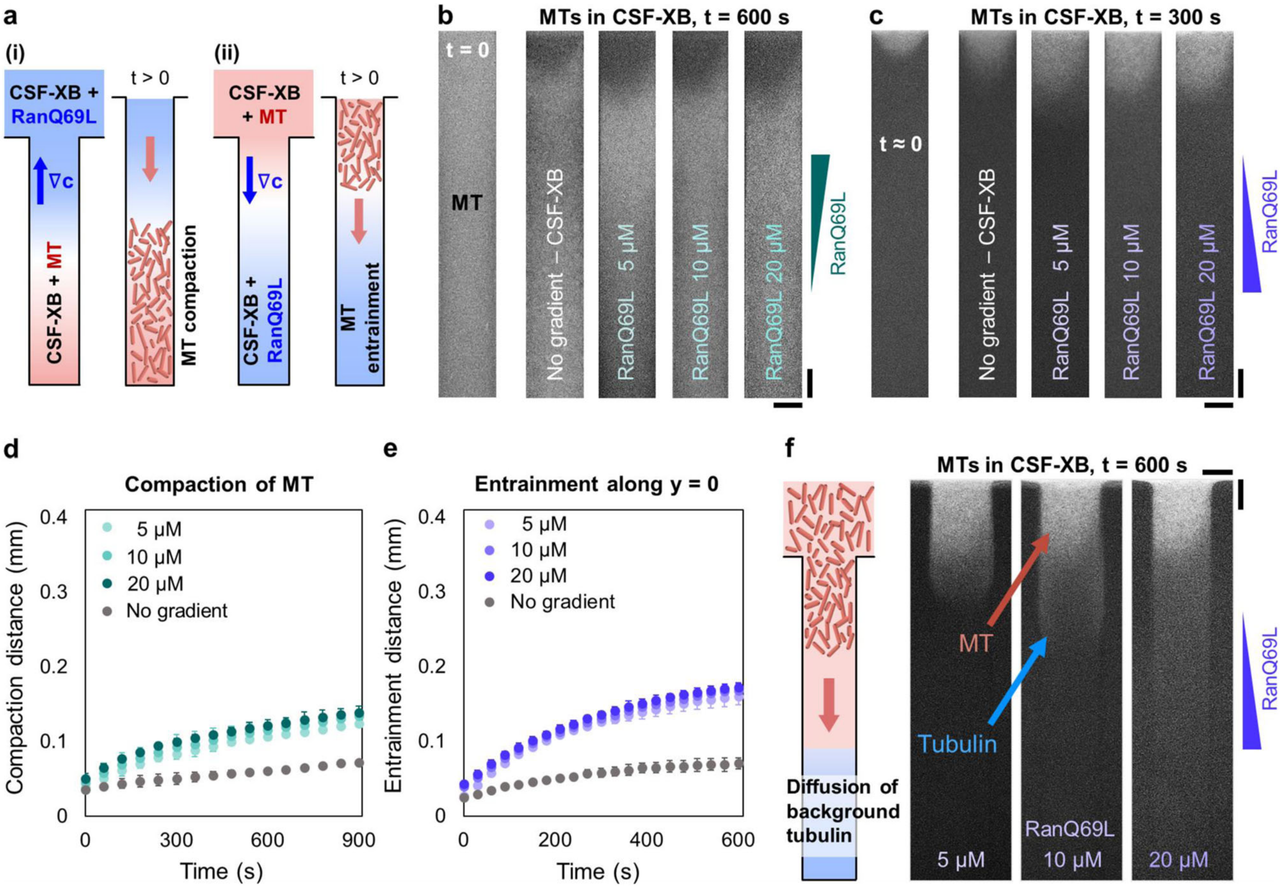

Fig. 4 | Diffusiophoresis of MTs under RanQ69L concentration gradients in CSF-XB. a Schematic of both compaction and entrainment experiments. Compaction and entrainment configurations are chosen to avoid direct contact of RanQ69L and MTs before $t = 0$. Experimental images of (**b**) compaction (negative gradient; $t = 600$ s) and (**c**) entrainment (positive gradient; $t = 300$ s) configurations. **d**, **e** Compaction and entrainment distances are plotted for different RanQ69L concentrations. There is only a slight concentration dependence and we observe no sign-change in the phoretic behavior of MTs. The no sign-change behavior is explained in the later section (Fig. 6d, e). **f** With higher contrast imaging, we observed not only the entrainment of MTs but also the background diffusion of depolymerized tubulin along a positive RanQ69L gradient. The diffusion behavior of background tubulin depends on the concentration of RanQ69L. **d**, **e** Data are presented as mean ± SD ($n = 15$ pores). All scale bars are 50 μm.

Tubulin- and RanQ69L-driven diffusiophoresis unraveled: long-range interaction in buffer and *Xenopus laevis* egg extract

We now present experiments with c-PS particles (radius R_{cPS}) and protein gradients to explain the tubulin-driven diffusiophoresis of MTs (Fig. 1) and the bi-directional behavior of RanQ69L-driven diffusiophoresis (Fig. 4). To begin, we use c-PS particles and CSF-XB buffer to perform experiments analogous with Fig. 1c. The pores are first filled with CSF-XB, and then the c-PS particles suspended with 0.4, 2, and 10 μM of tubulin (in CSF-XB) are flowed into the channel. We observe the entrainment of c-PS particles (Fig. 6a) into the pores, which is similar to the behavior of MTs (Fig. 1c). The entrainment distance along $y = 40$ μm is plotted versus time in order to exclude the effect of background flow v_F in the analysis (Fig. 6b). The squared entrainment distance (Fig. 6b; inset) is linear in time, showing the diffusive nature of diffusiophoresis. Tubulin-driven diffusiophoresis cannot be explained with standard electrolyte-driven diffusiophoresis theory (see SI for details) since tubulin does not behave like small ions ($R_{\mathrm{tub}} > \lambda_D$).

In the tubulin diffusion experiments (Fig. 5a, c), the behavior of tubulin was not influenced by the background ions and buffering agents. Therefore, for tubulin-driven diffusiophoresis, we only consider the diffusion of tubulin, without considering the coupled transport among all species. The diffusiophoretic velocity is related to the osmotic flow generated along the particle surface within an interaction length scale $\lambda_I (\ll R_{\mathrm{cPS}})$. Considering the repulsive interaction between tubulin and c-PS (or MTs), the diffusiophoretic velocity is (see SI for details)[10,13,46,64]

$$u_{DP} = -\lambda_I^2 \frac{k_B T}{2\mu} \frac{\partial c_{\mathrm{T}}}{\partial x}, \tag{3}$$

where c_{T} is the tubulin concentration obtained by solving a diffusion equation. The trajectory along $y = 40$ μm follows $\frac{dx_p}{dt} = u_{DP}(x_p, t)$. We compare the measured trajectories for c-PS and MTs (data from Fig. 1f) with the calculations using λ_I as a fitting parameter (Fig. 6b, c). The values of λ_I are included in the SI and Fig. 6. Although this calculation does not fully describe the flow field adjacent to the particle surface, we confirm that the scale of $\lambda_I = O(10\text{–}100)$ nm (and the trend) is consistent with the average separation distance $d_{\mathrm{tub}} = O(10\text{–}100)$ nm among micromolar tubulin molecules (see SI for details).

From this analysis we conclude that tubulin-driven diffusiophoresis of MTs (and c-PS) occurs due to the repulsive interaction between the tubulin molecules and MTs (or c-PS), both of which have a negative surface potential. In BRB80, the diffusiophoretic velocity of MTs was smaller (Fig. 1e, see SI), influenced by the lower surface potential of both MT and tubulin at pH 6.8. The surface potential argument is further supported by a control experiment (Fig. E4; see SI) using amine-modified polystyrene particles (a-PS; positively charged), where the a-PS particles migrate up the tubulin gradient. MTs and c-PS

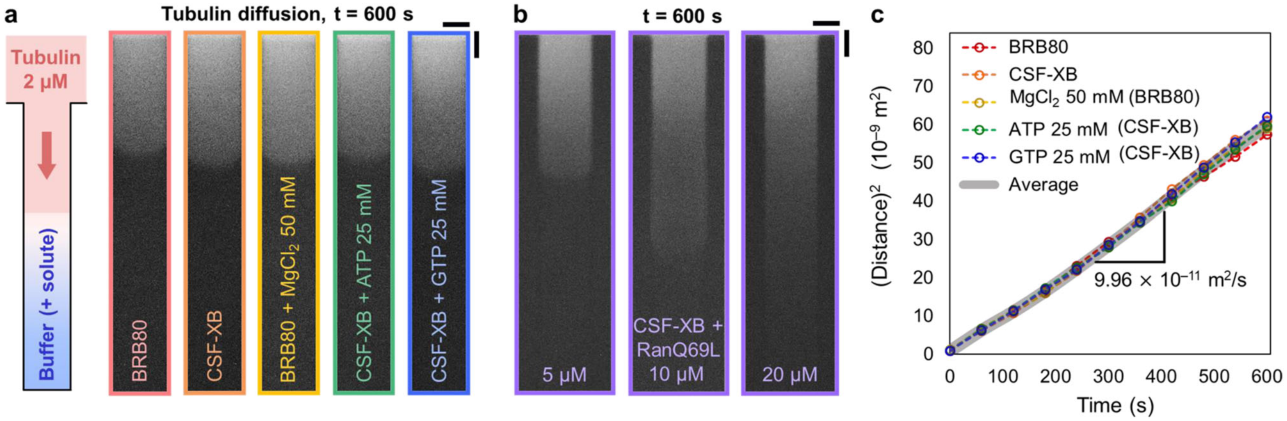

Fig. 5 | Diffusion of soluble tubulin under various conditions. a, **b** Diffusive entrainment of soluble tubulin (tagged with Alexa Fluor 568; solutions free of MTs) under eight different conditions. **a** Tubulin diffusion was not affected by the concentration gradients of MgCl$_2$, Mg-ATP, and Mg-GTP in BRB80 and CSF-XB buffers. **b** Tubulin diffusion depends on the concentration gradient of RanQ69L. **c** The squared entrainment trajectories are plotted versus time (except for the RanQ69L experiments), showing the slope as the tubulin diffusion coefficient (≈10^{-10} m^2/s). Data are presented as mean ± SD ($n = 20$ pores). The intensity profiles for tubulin diffusion under RanQ69L gradients are included in Fig. E3 (see SI). Scale bars are 50 μm.

particles behave analogously under both tubulin and MgCl$_2$ gradients as the role of surface potential is the major contribution to their diffusiophoretic transport. We henceforth use c-PS particles for control experiments to predict the behavior of MTs in more complex environments. In the study by Ramm et al.[18], the pattern formation of membrane cargo along the fluxes of MinDE protein was also interpreted as protein-driven diffusiophoresis, but induced by the steric hard-sphere interactions between cargo and MinDE. Evidently, the driving origin of diffusiophoresis can be different depending on the types of interactions between particles and solutes.

Next, we explain the puzzling behavior of MTs under negative and positive RanQ69L gradients (Fig. 4). Under a RanQ69L gradient alone in CSF-XB, c-PS particles migrated downhill by diffusiophoresis (Fig. 6d; see Fig. S14 for measurements and model calculations). RanGTP is negatively charged in CSF-XB (pH = 7.7), and a long-range repulsion is present between RanQ69L and c-PS (or MTs). Therefore, if there is no background depolymerized tubulin, MTs are also expected to migrate in the direction of negative RanQ69L gradient. When a positive RanQ69L gradient is formed into the pore, the c-PS particles stay within the inlet region, by slight penetration due to the flow in the main channel (Fig. 6e(i)-1, e(ii)-1). We observe that only in the presence of the cross-diffusion of tubulin and RanQ69L as illustrated in Fig. 6e(i)-2, e(ii)-2, c-PS particles migrated in the direction of the positive RanQ69L gradient. We conclude that the presence and diffusion of depolymerized tubulin affects the diffusiophoretic behavior of MTs in a RanGTP gradient in Fig. 4. As a consequence, it had appeared that MTs could move in both negative and positive gradients of RanQ69L in Fig. 4. The higher the concentration of RanQ69L, the stronger the depolymerization and diffusion of the background tubulin. Therefore, the cross-diffusion argument is consistent with the observation in Fig. 4.

Finally, we ask whether such diffusiophoretic effects can manifest in an active cytoplasmic environment and contribute to intracellular transport. Using *Xenopus laevis* egg extract, we tested diffusiophoresis of c-PS particles under MgCl$_2$ (Fig. 6f), tubulin, and RanQ69L (Fig. 6g) gradients. For this set of experiments, nocodazole (0.5 μg/mL) is included in the extract to prevent polymerization of tubulin. The effect of MgCl$_2$ gradients is reduced in *Xenopus laevis* egg extract compared to buffers, but the concentration dependence of the c-PS diffusiophoresis is maintained. The reduced diffusiophoretic speeds can be due to the interaction of MgCl$_2$ with other background species in the extract or simply due to the higher cytoplasmic viscosity that c-PS particles experience. We further confirm that tubulin and RanQ69L gradients induce diffusiophoresis of c-PS particles in the extract in the same direction as in buffers (Fig. 6g).

Intracellular species interactions are highly influenced by the system's physical chemistry. For example, tubulin and RanQ69L showed concentration dependent cross-diffusion in CSF-XB (Fig. 5b), but such a concentration dependence was largely reduced in the *Xenopus laevis* egg extract (Fig. S16). Therefore, a further investigation is required to make any general statements about intracellular diffusiophoresis. Nonetheless, from our study it can be concluded that micromolar concentration gradients of tubulin and RanGTP can drive diffusiophoresis of charged particles in an active cytoplasmic environment. Since the analogy between c-PS particles and MTs holds for tubulin- and RanQ69L-driven diffusiophoresis, we conclude that MT diffusiophoresis can contribute in driving intracellular MT transport whenever there are concentration gradients of tubulin and RanGTP, which is true in particular during mitosis and spindle assembly.

We discovered that MTs undergo diffusiophoresis along concentration gradients of soluble tubulin, MgCl$_2$, Mg-ATP, Mg-GTP, and RanGTP, and rationalized the observations using electrolyte- and non-electrolyte-driven diffusiophoresis theory. By identifying MT interactions with all system elements and demonstrating diffusiophoresis in *Xenopus laevis* egg extracts, we establish the feasibility of MT diffusiophoresis in cells. The diffusiophoretic velocity of MTs ($O(0.1)$ μm/s) obtained under the gradients of micromolar proteins and millimolar Mg-salts is comparable to the motor-driven MT transport speeds. Thus, diffusiophoresis can be significant in spindle assembly and other intracellular processes.

In order to fully describe the origin of protein-driven diffusiophoresis, surface interactions of proteins (e.g., tubulin, RanGTP, RanGDP, etc.; see SI), and MTs with other background species must be unraveled. Analyzing the flow field around MTs is also important. With an interaction distance of $O(100)$ nm, unlike the case with a small Debye length $O(0.1)$ nm for electrolytes, the non-electrolyte-driven diffusiophoresis must be shape-dependent. Follow-up in vitro studies considering the diffusiophoresis of dynamic MTs, as well as in vivo studies visualizing the transport of MTs along tubulin concentration gradients, can further extend the boundaries of our understanding of MT diffusiophoresis.

Our findings provide a concrete answer to the question of whether diffusiophoresis of charged macromolecules is possible in the cytoplasm. As discussed throughout the article, diffusiophoresis is a surface-flow-driven phenomenon and is determined by the coupled movements of solutes, particles, and fluids. Therefore, as

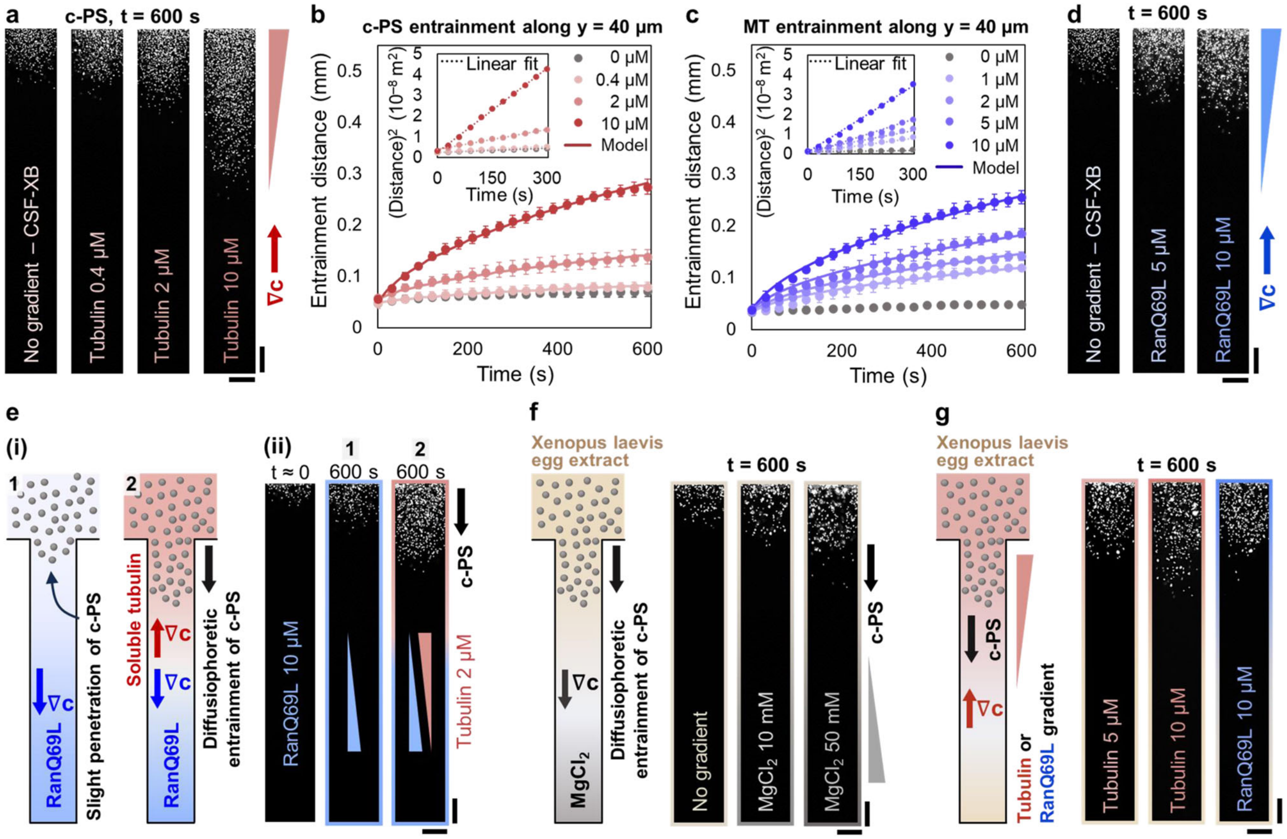

Fig. 6 | Tubulin- and RanQ69L-driven diffusiophoresis explained and demonstrated in active cytoplasmic environment using *Xenopus laevis* egg extract. **a** Diffusiophoresis of c-PS particles under tubulin gradients in CSF-XB. The entrainment distance is plotted versus time and fitted with the non-electrolyte diffusiophoresis model (eqn. (3); see SI for details) for (**b**) c-PS particles and (**c**) MTs. Insets: squared entrainment distance plotted versus time. Interaction length scale λ_I is used as a fitting parameter in the non-electrolyte diffusiophoresis model. Data are presented as mean ± SD ($n = 23$ pores). **b** For the tubulin concentrations 0.4, 2, and 10 μM, the value of λ_I are, respectively, 174 nm, 128 nm, and 105 nm. **c** For the tubulin concentrations 1, 2, 5, and 10 μM, the values of λ_I are, respectively, 174 nm, 142 nm, 105 nm, and 98 nm. **d** Without any influence of the background tubulin, the c-PS particles migrate down the RanQ69L gradient by diffusiophoresis. **e** Effect of cross-diffusion between tubulin and RanQ69L on c-PS diffusiophoresis (in CSF-XB). (**i-1**) Schematic describing an entrainment setup where a positive concentration gradient of RanQ69L is set toward the dead-end of the pore. There is no diffusiophoretic entrainment. (**i-2**) Schematic describing the entrainment setup with the cross-diffusion between 2 μM tubulin and 10 μM RanQ69L. (**ii**) Experimental images show that diffusiophoretic entrainment of c-PS particles toward high concentration RanQ69L only occurs when there is cross-diffusion of tubulin and RanQ69L. This can explain the behavior of MTs shown in Fig. 4. **f** Diffusiophoresis of c-PS particles under $MgCl_2$ gradient in *Xenopus laevis* egg extract. There is concentration-dependent entrainment of c-PS particles, with smaller penetration distance (than in BRB80 buffer) due to the crowdedness of the extract. **g** Diffusiophoresis of c-PS particles under tubulin and RanQ69L gradients in *Xenopus laevis* egg extract. All scale bars are 50 μm.

concentration gradients of ions, proteins, and other macromolecules are common in cells, diffusiophoretic transport may be ubiquitous in cells and we expect future studies to reveal additional instances of intracellular diffusiophoresis. Of course, systematic investigations identifying various combinations of particles, solutes, and the motion of the surrounding fluid are necessary for making general statements about diffusiophoresis in cells.

Methods

Ethics

Animal care was done in accordance with recommendations in the Guide for the Care and Use of Laboratory Animals of the NIH and the approved Institutional Animal Care and Use Committee (IACUC) protocol 1941 of Princeton University.

Microfluidic channel with a dead-end pore geometry

Microfluidic channels are made with PDMS (polydimethylsiloxane) using standard soft lithography. Between the molded PDMS and the glass slide, a thin layer of PDMS (1 mm) is also attached. In this way, we can make all four walls of the dead-end pores be PDMS and have the same surface property. The width, height, and length of the pores are, respectively, $w = 100$ μm, $h = 50$ μm, and $\ell = 1$ mm. For the main channel, width, height, and the length are, respectively, $W = 750$ μm, $H = 150$ μm, and $\ell = 5$ cm. For all experiments, the pores are initially filled with the first liquid, and followed by an air bubble, the second liquid is flowed in the main channel at a mean flow speed $\langle u \rangle = 1$ mm/s. Immediately after the two liquids contact with each other at the pore inlet, the flow speed in the main channel is decreased to $\langle u \rangle = 50$ μm/s. Images of the pores are recorded with an inverted microscope (Leica DMI4000B; 0.3 NA and 10x magnification, DFC360 FX camera with LAS AF software). For the images included in Fig. 2c, Nikon Ti-E microscope (1.49 NA and 100x magnification, Andor Zyla sCMOS camera with NIS elements software) is used.

Entrainment and compaction configurations

Main experiments for the diffusiophoresis of MTs and carboxylate-modified polystyrene (c-PS) particles are done in the entrainment configuration; MTs or c-PS particles are suspended in the second liquid. For some experiments demonstrating MT motion under biological solute gradients (of Mg-ATP, Mg-GTP, and RanQ69L), a compaction configuration is chosen. For compaction experiments, MTs are suspended in the first liquid, and the gradient-creating solutes are put in the second liquid. In this way, we can make the MTs meet the solutes after $t = 0$, and demonstrate the MT transport toward the dead-end of the pores for $t > 0$. Graphical descriptions for entrainment and compaction configurations can be found in[74].

Polystyrene particles

We used c-PS microspheres with a diameter $d = 1\,\mu m$ as model negatively charged particles. The c-PS particles are purchased from Thermo Fisher Scientific (F8820; Lot 2329001). The original c-PS particle suspension is diluted (final concentration 0.03 %v/v) in buffers (BRB80 or CSF-XB) or *Xenopus laevis* egg extract for use. For control experiments testing the positive surface potential (Fig. E4; see SI), amine-modified polystyrene (a-PS; $d = 1\,\mu m$) particles are used. The a-PS particles are purchased from Sigma Aldrich (L9654; Lot MKCQ2812), and the original suspension is diluted (final concentration 0.02 %v/v) in the CSF-XB buffer for use.

Protein expression and purification (RanQ69L and soluble tubulin)

Expression and purification of RanQ69L (Strep-6xHis-TEV-BFP-RanQ69L) was done following a previous protocol[88]. Briefly, RanQ69L was expressed in Rosetta2 E. coli cells and then lysed in lysis buffer (100 mM tris-HCl, pH 8.0, 450 mM NaCl, 1 mM $MgCl_2$, 1 mM EDTA, 0.5 mM PMSF, 6 mM BME, 200 μM GTP, 1 cOmplete^{TM} EDTA-free Protease Inhibitor, 1000 U DNAse 1). Protein was then affinity purified from lysate using a StrepTrap HP 5 mL column (GE Healthcare) in binding buffer (100 mM tris-HCl, pH 8.0, 450 mM NaCl, 1 mM $MgCl_2$, 1 mM EDTA, 6 mM BME, 200 μM GTP). Bound protein was eluted using elution buffer (100 mM tris-HCl, pH 8.0, 450 mM NaCl, 1 mM $MgCl_2$, 1 mM EDTA, 6 mM BME, 200 μM GTP, 2.5 mM D-desthiobiotin). Finally, eluted protein was dialyzed into CSF-XB (10 mM K-HEPES, 1 mM $MgCl_2$, 100 mM KCl, 5 mM K-EGTA, pH 7.7) + 10% (w/v) sucrose overnight. The dialysis product was then spun concentrated to 200 μM, aliquoted, and flash frozen.

Commercial tubulin from bovine brain (PurSolutions) was used for all experiments containing soluble tubulin or MTs. Labeling with Alexa-568 dye was done following a previous protocol[89].

RanQ69L and soluble tubulin were diluted to their desired concentrations using CSF-XB, CSF-XB + 10 % (w/v) sucrose, or BRB80 (80 mM K-PIPES, 1 mM $MgCl_2$, 1 mM EGTA, pH 6.8) depending on the experimental conditions.

Microtubule preparation

To make GMPCPP-stabilized, Alexa-568 labeled MT seeds, a 40 μL mixture of 20 μM bovine tubulin (10 % labeled with Alexa-568 dye) and 1 mM GMPCPP in BRB80 was polymerized for 45 min in a 37 °C water bath and centrifuged at 16000 × g for 8 min at room temperature in a tabletop centrifuge (Eppendorf). The supernatant was discarded and the seeds were resuspended with room temperature BRB80. The seeds were further diluted by 1/10 in BRB80 or CSF-XB for experiments, and the resulting MT supsension is used the same day.

To create Taxol-stabilized seeds (see SI), we adapted a protocol available from Tim Mitchison's lab. Briefly, a mixture of 20 μM tubulin (10% Alexa568-labeled tubulin) in BRB80 containing 1 mM GTP was prepared and incubated on ice for 5 min. The mixture was pre-cleared by ultracentrifugation, and the supernatant incubated at 37 °C for 2 min to initiate MT formation. 1/10 volumes of Taxol solutions in DMSO (2 μM, 20 μM, and 200 μM) were added to the mix stepwise, incubating at 37 °C for 10–15 min after each Taxol addition. After the last incubation, MTs were pelleted by centrifugation and resuspended in warm BRB80 containing 20 μM Taxol.

Xenopus laevis egg extract preparation

Meiotic *Xenopus laevis* egg extract was prepared as previously described[90] and then flash frozen. On experiment day, extract was thawed slowly on ice and supplemented with 0.5 μg/mL nocodazole to prevent MT polymerization.

$MgCl_2$, Mg-ATP and Mg-GTP experiments

For the experiments testing $MgCl_2$-, Mg-ATP-, and Mg-GTP-driven diffusiophoresis, desired concentrations of $MgCl_2$, Mg-ATP salt, and Mg-GTP salt are directly dissoved in the buffer (BRB80 or CSF-XB). MT or c-PS suspensions are prepared separately in the matching buffers, and the experiments are conducted either in the entrainment or compaction configurations.

RanQ69L experiments

RanQ69L was diluted in CSF-XB for the diffusiophoresis experiments (for MTs and c-PS particles; Figs. 4, 6d, e and Fig. S14) and the tubulin diffusion experiments (Fig. 5b). For the experiment done in *Xenopus laevis* egg extract (Fig. 6g), RanQ69L was diluted in the extract (second liquid for entrainment configuration). In order to match the crowdedness, the same proportion of CSF-XB + 10 % (w/v) sucrose was added in the extract that was used for the first liquid (initial pore-filling liquid).

Xenopus laevis egg extract experiments

Xenopus laevis egg extract is used for testing the c-PS diffusiophoresis under $MgCl_2$, tubulin and RanQ69L gradients (Fig. 6f, g). Also, the cross-diffusion between tubulin and RanQ69L is observed using the extract (Fig. S16). The solutes are initially prepared at higher concentrations in CSF-XB + 10 % (w/v) sucrose, and diluted to desired concentrations in the *Xenopus laevis* egg extracts. The first and second liquids in the experiments had matching crowdedness by adding the same amount of CSF-XB + 10 % (w/v) sucrose in the *Xenopus laevis* egg extract.

TIRF assays for GMPCPP- and Taxol-stabilized MTs

For TIRF assays, fresh MT seeds (GMPCPP- and Taxol-stabilized) were made. The MT seeds contained 10 % biotin-labeled tubulin in addition to 10 % ATTO647N-labeled tubulin. Imaging flow chambers were created by securing strips of double-sided tape onto microscope slides (~2 cm apart) and securing untreated coverslips atop the tape. A solution of 0.1 mg/mL anti-biotin antibody (Invitrogen: Z021) diluted in BRB80 was flowed into the chambers and incubated at room temperature for 10 min. MTs were then freshly diluted in BRB80 (1:500 for taxol seeds and 1:750 for GMPCPP seeds), flowed into the chamber, and incubated for 10 min at room temperature. Then, CSF-XB (0 % sucrose) and 10 μM RanQ69L freshly diluted in CSF-XB, respectively, are flowed into the imaging chamber, and the MTs are imaged immediately. All buffers for Taxol-stabilized seeds contained 20 μM Taxol. Images were captured every minute for 15 min using a Nikon Ti-E inverted system (RRID:SCR021242) with an Apo TIRF 100x oil objective (NA = 1.49), and an Andor Neo Zyla (VSC-04209) camera. Exposure settings of 400 ms and 200 ms (647 laser) were used to image the GMPCPP- and Taxol-stabilized MTs, respectively.

Reporting summary

Further information on research design is available in the Nature Portfolio Reporting Summary linked to this article.

Data availability

The data supporting the findings of this study are available within the paper and its Supplementary Information. Source data are provided with this paper.

Code availability

Sufficient details and explanations of the code used for model calculations are provided in the SI. The code is available from the corresponding authors upon request.

References

1. Anderson, J. L. Transport mechanisms of biological colloids. *Ann. N. Y. Acad. Sci.* **469**, 166–177 (1986).
2. Agutter, P. S. & Whetley, D. N. Random walks and cell size. *Bioessays* **22**, 1018–1023 (2000).
3. Mikhailov, A. S. & Kapral, R. Hydrodynamic collective effects of active protein machines in solution and lipid bilayers. *Proc. Natl. Acad. Sci. USA* **112**, E3639–E3644 (2015).
4. Walter, J.-C. proteophoresis as a mechanism for bacterial genome partitioning. *Phys. Rev. Lett.* **119**, 028–101 (2017).
5. Ramm, B. et al. The MinDE system is a generic spatial cue for membrane protein distribution in vitro. *Nat. Commun.* **9**, 39–42 (2018).
6. Derjaguin, B. V., Sidorenkov, G. P., Zubashchenkov, E. A. & Kiseleva, E. V. Kinetic phenomena in the boundary layers of liquids 1. *Kolloidn. Zh.* **9**, 335–347 (1947).
7. Derjaguin, B. V., Sidorenkov, G. P., Zubashchenkov, E. A. & Kiseleva, E. V. Kinetic phenomena in the boundary layers of liquids 1. *Prog. Surf. Sci.* **43**, 138–152 (1993).
8. Derjaguin, B. V., Dukhin, S. S. & Korotkova, A. A. Diffusiophoresis in electrolyte solutions and its role in the mechanism of film formation from rubber latexes by the method of ionic deposition. *Kolloidn. Zh.* **23**, 53–58 (1961).
9. Derjaguin, B. V., Dukhin, S. S. & Korotkova, A. A. Diffusiophoresis in electrolyte solutions and its role in the mechanism of film formation from rubber latexes by the method of ionic deposition. *Prog. Surf. Sci.* **43**, 153–158 (1993).
10. Anderson, J. L., Lowell, M. E. & Prieve, D. C. Motion of a particle generated by chemical gradients. *J. Fluid Mech.* **117**, 107–121 (1982).
11. Dukhin, S. S., Ul'berg, Z. R., Dvornichenko, G. L. & Derjaguin, B. V. Diffusiophoresis in electrolyte solutions and its application to the formation of surface coatings. *Russ. Chem. Bull.* **31**, 1535–1544 (1982).
12. Prieve, D. C., Anderson, J. L., Ebel, J. P. & Lowell, M. E. Motion of a particle generated by chemical gradients. Part 2. Electrolytes. *J. Fluid Mech.* **148**, 247–269 (1984).
13. Anderson, J. L. & Prieve, D. C. Diffusiophoresis: migration of colloidal particles in gradients of solute concentration. *Sep. Purif. Methods* **13**, 67–103 (1984).
14. Ebel, J. P., Anderson, J. L. & Prieve, D. C. Diffusiophoresis of latex particles in electrolyte gradients. *Langmuir* **4**, 396–406 (1988).
15. Anderson, J. L. Colloid transport by interfacial forces. *Annu. Rev. Fluid Mech.* **21**, 61–99 (1989).
16. Dukhin, S. Non-equilibrium electric surface phenomena. *Adv. Colloid Interface Sci.* **44**, 1–134 (1993).
17. Sear, R. P. A general nonequilibrium, nonmotor mechanism for the metabolism-dependent transport of particles in cells. *Phys. Rev. Lett.* **122**, 128–101 (2019).
18. Ramm, B. et al. A diffusiophoretic mechanism for ATP-driven transport without motor proteins. *Nat. Phys.* **17**, 850–858 (2021).
19. Häfner, G. & Müller, M. Reaction-driven diffusiophoresis of diquid condensates: potential mechanisms for intracellular organization. *ACS Nano* **18**, 16530–16544 (2024).
20. Ledbetter, M. C. & Porter, K. R. A "microtubule" in plant cell fine structure. *J. Cell Biol.* **19**, 239–250 (1963).
21. Wühr, M. et al. Evidence for an upper limit to mitotic spindle length. *Curr. Biol.* **18**, 1256–1261 (2008).
22. Hayashi, H., Kimura, K. & Kimura, A. Localized accumulation of tubulin during semi-open mitosis in the *Caenorhabditis elegans* embryo. *Mol. Biol. Cell.* **23**, 1688–1699 (2012).
23. Woodruff, J. B. et al. The centrosome is a selective condensate that nucleates microtubules by concentrating tubulin. *Cell* **169**, 1066–1077 (2017).
24. Baumgart, J. et al. Soluble tubulin is significantly enriched at mitotic centrosomes. *J. Cell. Biol.* **218**, 3977–3985 (2019).
25. Petry, S. Mechanisms of mitotic spindle assembly. *Annu. Rev. Biochem.* **85**, 659–683 (2016).
26. Brugués, J., Nuzzo, V., Mazur, E. & Needleman, D. J. Nucleation and transport organize microtubules in metaphase spindles. *Cell* **149**, 554–564 (2012).
27. Alfaro-Aco, R. & Petry, S. Building the microtubule cytoskeleton piece by piece. *J. Biol. Chem.* **290**, 17154–17162 (2015).
28. Silverman-Gavrila, R. V. & Wilde, A. Ran is required before metaphase for spindle assembly and chromosome alignment and after metaphase for chromosome segregation and spindle midbody organization. *Mol. Biol. Cell.* **17**, 2069–2080 (2006).
29. Martin, S. R., Butler, F. M. M., Clark, D. C., Zhou, J.-M. & Bayley, P. M. Magnesium ion effects on microtubule nucleation in vitro. *Biochim. Biophys. Acta Protein Struct. Mol. Enzymol.* **914**, 96–100 (1987).
30. Grover, S. & Hamel, E. The magnesium-GTP interaction in microtubule assembly. *Eur. J. Biochem.* **222**, 163–172 (1994).
31. Uz, G. & Sarikaya, A. T. The effect of magnesium on mitotic spindle formation in Schizosaccharomyces pombe. *Genet. Mol. Biol.* **39**, 459–464 (2016).
32. Goodson, H. V. & Jonasson, E. M. Microtubules and microtubule-associated proteins. *Cold Spring Harb. Perspect. Biol.* **10**, a022608 (2018).
33. Prosser, S. L. & Pelletier, L. Mitotic spindle assembly in animal cells: a fine balancing act. *Nat. Rev. Mol. Cell Biol.* **18**, 187–201 (2017).
34. Clarke, P. R. A gradient signal orchestrates the mitotic spindle. *Science* **309**, 1334–1335 (2005).
35. Clarke, P. R. & Zhang, C. Spatial and temporal coordination of mitosis by Ran GTPase. *Nat. Rev. Mol. Cell Biol.* **9**, 464–477 (2008).
36. Kalab, P. & Heald, R. The RanGTP gradient – a GPS for the mitotic spindle. *J. Cell Sci.* **121**, 1577–1586 (2008).
37. Cesario, J. & McKim, K. RanGTP is required for meiotic spindle organization and the initiation of embryonic development in Drosophila. *J. Cell Sci.* **124**, 3797–3810 (2011).
38. Oh, D., Yu, C.-H. & Needleman, D. J. Spatial organization of the Ran pathway by microtubules in mitosis. *Proc. Natl. Acad. Sci. USA* **113**, 8729–8734 (2016).
39. Lavia, P. The GTPase RAN regulates multiple steps of the centrosome life cycle. *Chromosome Res.* **24**, 53–65 (2016).
40. Popescu, M. N., Uspal, W. E., Bechinger, C. & Fischer, P. Chemotaxis of active Janus nanoparticles. *Nano Lett.* **18**, 5345–5349 (2018).
41. Ramachandran, A. & Santiago, J. G. Isotachophoresis: theory and microfluidic applications. *Chem. Rev.* **122**, 12904–12976 (2022).
42. Shim, S. Diffusiophoresis, diffusioosmosis, and microfluidics: surface-flow-driven phenomena in the presence of flow. *Chem. Rev.* **122**, 6986–7009 (2022).
43. Gu, Y., Tran, L., Lee, S., Zhang, J. & Bishop, K. J. Convection confounds measurements of osmophoresis for lipid vesicles in solute gradients. *Langmuir* **39**, 942–948 (2023).
44. Ganguly, A., Alessio, B. M. & Gupta, A. Diffusiophoresis: a novel transport mechanism-fundamentals, applications, and future opportunities. *Front. Sens.* **4**, 1322906 (2023).
45. Velegol, D., Garg, A., Guha, R., Kar, A. & Kumar, M. Origins of concentration gradients for diffusiophoresis. *Soft Matter* **12**, 4686–4703 (2016).
46. Marbach, S. & Bocquet, L. Osmosis, from molecular insights to large-scale applications. *Chem. Soc. Rev.* **48**, 3102–3144 (2019).
47. Abécassis, B., Cottin-Bizonne, C., Ybert, C., Ajdari, A. & Bocquet, L. Boosting migration of large particles by solute contrasts. *Nat. Mater.* **7**, 785–789 (2008).
48. Shin, S. et al. Size-dependent control of colloid transport via solute gradients in dead-end channels. *Proc. Natl. Acad. Sci. USA* **113**, 257–261 (2016).
49. Shim, S. et al. CO_2-driven diffusiophoresis for maintaining a bacteria-free surface. *Soft Matter* **17**, 2568–2576 (2021).

50. Florea, D., Musa, S., Huyghe, J. & Wyss, H. Long-range repulsion of colloids driven by ion exchange and diffusiophoresis. *Proc. Natl. Acad. Sci. USA* **111**, 6554–6559 (2014).
51. Shi, N., Nery-Azevedo, R., Abdel-Fattah, A. I. & Squires, T. M. Diffusiophoretic focusing of suspended colloids. *Phys. Rev. Lett.* **117**, 258001 (2016).
52. Banjeree, A., Williams, I., Nery-Azevedo, R., Helgeson, M. E. & Squires, T. M. Soluto-inertial phenomena: Designing long-range, long-lasting, surface-specific interactions in suspensions. *Proc. Natl. Acad. Sci. USA* **113**, 8612–8617 (2016).
53. Vrhovec Hartman, S., Božič, B. & Derganc, J. Migration of blood cells and phospholipid vesicles induced by concentration gradients in microcavities. *N. Biotechnol.* **47**, 60–66 (2018).
54. Palacci, J., Abécassis, B., Cottin-Bizonne, C., Ybert, C. & Bocquet, L. Colloidal motility and pattern formation under rectified diffusiophoresis. *Phys. Rev. Lett.* **104**, 138302 (2010).
55. Rasmussen, M. K., Pedersen, J. N. & Marie, R. Size and surface charge characterization of nanoparticles with a salt gradient. *Nat. Commun.* **11**, 2338 (2020).
56. Annunziata, O., Buzatu, D. & Albright, J. G. Protein diffusiophoresis and salt osmotic diffusion in aqueous solutions. *J. Phys. Chem. B.* **116**, 12694–12705 (2012).
57. Shim, S. & Stone, H. A. CO2-leakage-driven diffusiophoresis causes spontaneous accumulation of charged materials in channel flow. *Proc. Natl. Acad. Sci. USA* **117**, 25985–25990 (2020).
58. Peter, Q. A. et al. Microscale diffusiophoresis of proteins. *J. Phys. Chem. B.* **126**, 8913–8920 (2022).
59. Somasundar, A., Qin, B., Shim, S., Bassler, B. L. & Stone, H. A. Diffusiophoretic particle penetration into bacterial biofilms. *ACS Appl. Mater. Interfaces* **15**, 33263–33272 (2023).
60. Kar, A., Chiang, T.-Y., Ortiz-Rivera, I., Sen, A. & Velegol, D. Enhanced transport into and out of dead-end pores. *ACS Nano* **9**, 746–753 (2015).
61. Battat, S., Ault, J. T., Shin, S., Khodaparast, S. & Stone, H. A. Particle entrainment in dead-end pores by diffusiophoresis. *Soft Matter* **15**, 3879–3885 (2019).
62. Gupta, A., Shim, S. & Stone, H. A. Diffusiophoresis: from dilute to concentrated electrolytes. *Soft Matter* **16**, 6975–6984 (2020).
63. Shim, S., Nunes, J. K., Chen, G. & Stone, H. A. Diffusiophoresis in the presence of a pH gradient. *Phys. Rev. Fluids* **7**, 110513 (2022).
64. Williams, I., Lee, S., Apriceno, A., Sear, R. P. & Battaglia, G. Diffusioosmotic and convective flows induced by a nonelectrolyte concentration gradient. *Proc. Natl. Acad. Sci. USA* **117**, 25263–25271 (2020).
65. Hong, J., Kim, B. & Shin, H. Mixed-scale poly (methyl methacrylate) channel network-based single-particle manipulation via diffusiophoresis. *Nanoscale* **10**, 14421–14431 (2018).
66. Lee, H., Kim, J., Yang, J., Seo, S. W. & Kim, S. J. Diffusiophoretic exclusion of colloidal particles for continuous water purification. *Lab Chip* **18**, 1713–1724 (2018).
67. Alessio, B. M. & Gupta, A. Diffusiophoresis-enhanced Turing patterns. *Sci. Adv.* **9**, eadj2457 (2023).
68. Ault, J. T., Shin, S. & Stone, H. A. Characterization of surface-solute interactions by diffusioosmosis. *Soft Matter* **15**, 1582–1596 (2019).
69. Alessio, B. M., Shim, S., Mintah, E., Gupta, A. & Stone, H. A. Diffusiophoresis and diffusioosmosis in tandem: two-dimensional particle motion in the presence of multiple electrolytes. *Phys. Rev. Fluids* **6**, 054201 (2021).
70. Alessio, B. M., Shim, S., Gupta, A. & Stone, H. A. Diffusioosmosis-driven dispersion of colloids: a Taylor dispersion analysis with experimental validation. *J. Fluid Mech.* **942**, A23 (2022).
71. Van den Heuvel, M. G. L., De Graaff, M. P. & Dekker, C. Molecular sorting by electrical steering of microtubules in kinesin-coated channels. *Science* **312**, 910–914 (2006).
72. Van den Heuvel, M. G. L., De Graaff, M. P., Lemay, S. G. & Dekker, C. Electrophoresis of individual microtubules in microchannels. *Proc. Natl. Acad. Sci. USA* **103**, 7770–7775 (2007).
73. Eatkins, B. B. et al. Modeling microtubule counterion distributions and conductivity using the Poisson-Boltzmann equation. *Front. Mol. Biosci.* **8**, 650757 (2021).
74. Wilson, J. L., Shim, S., Yu, Y. E., Gupta, A. & Stone, H. A. Diffusiophoresis in multivalent electrolytes. *Langmuir* **36**, 7014–7020 (2020).
75. Kirby, B. J. & Hasselbrink Jr, E. F. Zeta potential of microfluidic substrates: 2. Data for polymers. *Electrophoresis* **25**, 203–213 (2004).
76. Gupta, A., Rallabandi, B. & Stone, H. A. Diffusiophoretic and diffusioosmotic velocities for mixtures of valence-asymmetric electrolytes. *Phys. Rev. Fluids* **4**, 043702 (2019).
77. Phillips, R. Adenosine and the adenine nucleotides. Ionization, metal complex formation, and conformation in solution. *Chem. Rev.* **66**, 501–527 (1966).
78. Wilson, J. E. & Chin, A. Chelation of divalent cations by ATP, studied by titration calorimetry. *Anal. Biochem.* **193**, 16–19 (1991).
79. Yamanaka, R. et al. Mitochondrial Mg^{2+} homeostasis decides cellular energy metabolism and vulnerability to stress. *Sci. Rep.* **6**, 30027 (2016).
80. Storer, A. C. & Cornish-Bowden, A. Concentration of $MgATP^{2-}$ and other ions in solution. Calculation of the true concentrations of species present in mixtures of associating ions. *Biochem. J.* **159**, 1–5 (1976).
81. Rudack, T., Xia, F., Schlitter, J., Kötting, C. & Gerwert, K. The role of magnesium for geometry and charge in GTP hydrolysis, revealed by quantum mechanics/molecular mechanics simulations. *Biochem. J.* **103**, 293–302 (2012).
82. Shandilya, E., Rallabandi, B. & Maiti, S. In situ enzymatic control of colloidal phoresis and catalysis through hydrolysis of ATP. *Nat. Commun.* **15**, 3603 (2024).
83. Miniowitz-Shemtov, S., Teichner, A., Sitry-Shevah, D. & Hershko, A. ATP is required for the release of the anaphase-promoting complex/cyclosome from inhibition by the mitotic checkpoint. *Proc. Natl. Acad. Sci. USA* **107**, 5351–5356 (2010).
84. Zhou, J. et al. Structural insights into the mechanism of GTP initiation of microtubule assembly. *Nat. Commun.* **14**, 5980 (2023).
85. Patel, A. et al. ATP as a biological hydrotrope. *Science* **356**, 753–756 (2017).
86. Mandelkow, E. & Mandelkow, E.-M. Microtubular structure and tubulin polymerization. *Curr. Opin. Cell Biol.* **1**, 5–9 (1989).
87. Deen, W. M. *Analysis of Transport Phenomena* (Oxford University Press, 2012).
88. King, M. & Petry, S., Visualizing and analyzing branching microtubule nucleation using meiotic *Xenopus* egg extracts and TIRF microscopy. *Methods Mol. Biol.* **1413**, 77–85 (2016).
89. Gell, C. et al. Microtubule dynamics reconstituted in vitro and imaged by single-molecule fluorescence microscopy. *Method. Cell Biol.* **95**, 221–245 (2010).
90. Good, M. C. & Heald, R. Preparation of cellular extracts from *Xenopus* eggs and embryos. *Cold Spring Harb. Protoc.* **2018**, pdbrot097055 (2018).

Acknowledgements

We thank Akanksha Thawani and Pedro de Souza for valuable discussions. We thank the NSF for support via grants CBET-2127563 (to H.A.S.) and PHY-1734030 (to B.R.).

Author contributions

S.S., B.G., S.P., and H.A.S. conceived the project. S.S. conducted all microfluidic experiments and numerical calculations. B.G. prepared all biological samples for the microfluidic experiments. V.A.V. conducted

TIRF assays and prepared all biological samples for the review experiments. S.S., B.G., B.R., S.P., and H.A.S. discussed the results, and all authors contributed to writing the manuscript.

Competing interests

The authors declare no competing interests.

Additional information

Supplementary information The online version contains supplementary material available at https://doi.org/10.1038/s41467-024-53656-w.

Correspondence and requests for materials should be addressed to Suin Shim or Howard A. Stone.

Peer review information *Nature Communications* thanks the anonymous reviewers for their contribution to the peer review of this work. A peer review file is available.

Reprints and permissions information is available at http://www.nature.com/reprints

Publisher's note Springer Nature remains neutral with regard to jurisdictional claims in published maps and institutional affiliations.

Open Access This article is licensed under a Creative Commons Attribution-NonCommercial-NoDerivatives 4.0 International License, which permits any non-commercial use, sharing, distribution and reproduction in any medium or format, as long as you give appropriate credit to the original author(s) and the source, provide a link to the Creative Commons licence, and indicate if you modified the licensed material. You do not have permission under this licence to share adapted material derived from this article or parts of it. The images or other third party material in this article are included in the article's Creative Commons licence, unless indicated otherwise in a credit line to the material. If material is not included in the article's Creative Commons licence and your intended use is not permitted by statutory regulation or exceeds the permitted use, you will need to obtain permission directly from the copyright holder. To view a copy of this licence, visit http://creativecommons.org/licenses/by-nc-nd/4.0/.

© The Author(s) 2024, corrected publication 2024